

# The Role of Vacancies in Oxide Detachment and Mechanical Degradation of Subsurface for AlCoCrFeNi Alloy at High Temperature

Gaosheng Yan, Zhiwen Bai, Fuhao Wang, Mengdie Lan, Yihan Wu,\* Wenshan Yu,\* and Shengping Shen\*

The protective function of the oxide scale and the vulnerability of the subsurface region play key roles in determining the high-temperature durability of AlCoCrFeNi high-entropy alloys (HEAs), yet their degradation mechanisms remain insufficiently understood. This study investigates the mechanisms of oxide scale spallation and subsurface mechanical degradation in the AlCoCrFeNi HEA after high-temperature oxidation at 1000 °C. Severe oxide scale spallation is not solely caused by residual stress but is closely linked to vacancy coalescence at the oxide/alloy interface, primarily induced by outward Al diffusion and the Kirkendall effect. A bilayer Al<sub>2</sub>O<sub>3</sub> scale ( $\approx 8.4 \mu\text{m}$  thick after 200 h oxidation) forms, consisting of equiaxed and columnar grains. Moreover, the subsurface region undergoes a body-centered cubic (BCC)-to-face-centered cubic (FCC) phase transformation, which reduces the diffusion coefficient of Al (from  $4.17 \times 10^{-11} \text{ m}^2 \text{ s}^{-1}$  in BCC to  $1.8 \times 10^{-11} \text{ m}^2 \text{ s}^{-1}$  in FCC), thereby enhancing oxidation resistance. Meanwhile, nanomechanical testing reveals an  $\approx 30\%$  reduction in yield strength in the subsurface layer, attributed to vacancy-induced reductions in stacking fault energy, which promote dislocation activity and plastic deformation. This study provides critical insights into the coupled effects of oxidation, vacancy dynamics, and phase transformation on the high-temperature performance of HEAs, offering valuable guidance for their application in extreme environments.

## 1. Introduction

In recent years, high-entropy alloys (HEAs) have attracted significant attention in the field of materials science due to their unique multiprincipal element design philosophy and

exceptional comprehensive properties.<sup>[1,2]</sup> Unlike conventional alloys, HEAs introduce multiple principal elements (typically five or more, with each element's atomic percentage ranging between 5% and 35%).<sup>[3]</sup> The combined effects (the high-entropy effect, sluggish diffusion effect, severe lattice distortion effect, and cocktail effect) endow HEAs with outstanding mechanical properties,<sup>[4]</sup> corrosion resistance, high-temperature performance, and oxidation resistance.<sup>[4–8]</sup> These remarkable characteristics make HEAs highly promising for potential applications in extreme environments such as aerospace, energy, and nuclear industries.<sup>[9–11]</sup>

AlCoCrFeNi HEA, as a representative HEA, features a dual-phase structure composed of a high degree of coherent A2 (disordered body-centered cubic (BCC)) and B2 (ordered BCC) phases.<sup>[12]</sup> This unique structural configuration ensures superior strength at elevated temperatures.<sup>[13]</sup> Additionally, compared to conventional superalloys, the AlCoCrFeNi HEA is relatively lightweight and cost-effective due to its high Al and Fe content.<sup>[14]</sup> Due to its

relatively low cost and excellent high-temperature properties, the AlCoCrFeNi HEA has become one of the most extensively studied HEAs with potential for practical applications. In addition, during its application, high-temperature oxidation is one of the most critical challenges that the AlCoCrFeNi HEA must face and endure.<sup>[15]</sup>

Extensive research has been conducted on the high-temperature oxidation behavior of AlCoCrFeNi HEA.<sup>[14,16–18]</sup> The results indicate that this HEA exhibits superior oxidation resistance compared to traditional Fe- and Ni-based alloys containing Al and Cr. The excellent oxidation resistance of AlCoCrFeNi HEA can be attributed to the sluggish diffusion effect of its constituent metallic elements.<sup>[18]</sup> The sluggish diffusion in AlCoCrFeNi HEA plays a crucial role in their oxidation behavior, as the growth of the oxide scale is a diffusion-controlled process according to classical oxidation theory.<sup>[19]</sup> Furthermore, during oxidation at temperatures ranging from 900 to 1100 °C, the oxide scale formed on AlCoCrFeNi HEA primarily consists of Al<sub>2</sub>O<sub>3</sub> with a bilayer structure comprising columnar and

G. Yan, Z. Bai, F. Wang, M. Lan, W. Yu, S. Shen  
State Key Laboratory for Strength and Vibration of Mechanical Structures  
School of Aerospace Engineering  
Xi'an Jiaotong University  
Xi'an 710049, P. R. China  
E-mail: wenshan@xjtu.edu.cn; sshen@xjtu.edu.cn

Y. Wu  
School of Mechanical Engineering and Automation  
Fuzhou University  
Fuzhou 350108, China  
E-mail: wuyihan@fzu.edu.cn

 The ORCID identification number(s) for the author(s) of this article can be found under <https://doi.org/10.1002/adem.202501118>.

DOI: 10.1002/adem.202501118

equiaxed grains.<sup>[18]</sup> The formation of this bilayer Al<sub>2</sub>O<sub>3</sub> is primarily governed by the differential diffusion rates of O and Al in oxide scale.<sup>[14]</sup> Clearly, these studies have comprehensively elucidated the diffusion behavior of elements and the oxidation resistance mechanism of AlCoCrFeNi HEAs during high-temperature oxidation.

However, experimental observations show that the oxide scale on the AlCoCrFeNi HEA is more prone to spallation. This behavior is in contrast to the oxide scales on conventional Fe- and Ni-based alloys.<sup>[20]</sup> In fact, the oxide scale formed on AlCoCrFeNi HEA exhibits unusually poor adhesion. Even mild mechanical disturbance, such as a gentle airflow, can cause large portions of the scale to detach spontaneously. Unfortunately, this phenomenon has not received sufficient attention from researchers. The explanation provided so far attributes the detachment of the oxide scale to the residual stresses present within it.<sup>[21]</sup> However, similar levels of residual stress are also present in the oxide scales formed on traditional Fe- and Ni-based alloys, yet those oxide scales exhibit strong adhesion to the underlying alloys.<sup>[22,23]</sup> Clearly, the residual stress alone is insufficient to fully explain this phenomenon. In addition to stress, the diffusion behavior of alloying elements and vacancies likely plays a critical role in oxide scale adhesion. Additionally, the microstructural evolution at the alloy surface during high-temperature oxidation also significantly influences the adhesion between oxide scale and alloy substrate.<sup>[24]</sup> Unfortunately, studies and analyses focusing on these aspects in the context of AlCoCrFeNi HEAs remain scarce. Therefore, the poor adhesion behavior between the oxide scale and the AlCoCrFeNi HEA substrate requires further investigation and validation to better understand the underlying mechanisms.

Generally, the oxide scale formed during oxidation does not possess load-bearing capability. This function remains the responsibility of the alloy material. The alloy subsurface, as the initial site for crack initiation, plays a critical role in determining the structural safety of the entire alloy.<sup>[25]</sup> Thus, investigating the compositional and structural evolution (e.g., depletion, segregation, phase transformation, and nanopores) of the alloy subsurface after oxidation, as well as their effects on the subsurface mechanical properties, is of significant importance. Notably, the changes in subsurface mechanical properties after oxidation depend on the type of alloy system. While some alloys show improved properties, others experience degradation.<sup>[26]</sup> For instance, in the case of refractory HEAs, the inward diffusion of oxygen in alloy during oxidation leads to the formation of O interstitial complexes, which enhances the mechanical properties of the subsurface.<sup>[27]</sup> Conversely, the oxidation of steel results in a deterioration of mechanical properties due to the production of vacancies at grain boundaries.<sup>[28]</sup> Thus, the subsurface mechanical properties of alloys are closely tied to the diffusion behavior of elements during the oxidation process. At present, limited research has been conducted on the mechanical properties of the subsurface in AlCoCrFeNi HEA after oxidation, particularly regarding its yield strength. Further investigations are needed to understand the relationship between oxidation-induced compositional and structural changes and the mechanical performance of the subsurface in this HEA system. In oxidation-prone environments, the subsurface region beneath the oxide scale plays a pivotal role in load-bearing and is often the

initial site for damage accumulation and crack initiation. Understanding how oxidation-induced changes affect its mechanical properties is therefore essential for improving alloy performance under extreme conditions.

The objective of this study is to investigate the underlying causes of the poor adhesion between the oxide scale and the HEA substrate, as well as the mechanical of the subsurface. To achieve these goals, the AlCoCrFeNi HEA is prepared and subjected to isothermal oxidation experiments in static air at 1000 °C for 200 h. Simultaneously, we analyze the evolution of the microstructure of the oxide scale, the oxide/alloy interface, the subsurface layer, and the bulk of AlCoCrFeNi HEA. Furthermore, the yield strength and deformation behavior of the subsurface in the AlCoCrFeNi HEA are evaluated using a nanomechanical testing system. These results are compared with the yield strength of the transformation phase zone in the AlCoCrFeNi HEA. This zone possesses a crystal structure similar to that of the tested subsurface. Finally, based on experimental observations and molecular dynamics (MD) simulation results, we analyze and discuss the following key aspects: 1) the growth mechanism of the bilayer oxide scale, 2) the formation of vacancies and their role in inducing low interface adhesion, and 3) the mechanical degradation mechanisms of the subsurface layer.

## 2. Results

### 2.1. Structure and Composition of the Original Alloy

Figure 1 illustrate the microstructure and chemical composition distribution of the as-cast AlCoCrFeNi HEA. As shown in Figure 1a,b, the microstructure consists of a grayish-black matrix region and white precipitate-like areas. According to the X-ray diffraction (XRD) analysis, the as-cast AlCoCrFeNi HEA contains only a BCC phase (Figure 1c). This suggests that both the grayish-black matrix and the white precipitate-like areas share a BCC structure, with the contrast differences arising from variations in elemental composition. However, the XRD results alone cannot distinguish between the two BCC phases. To address this limitation, further transmission electron microscope (TEM) analysis is performed. TEM combined with selected area electron diffraction (SAED) confirms that the continuous grayish-black matrix corresponds to an ordered BCC (B2) structure (Figure 1d–f), while the white precipitate-like areas correspond to a disordered BCC (A2) structure. The formation of this microstructure is attributed to a spinodal decomposition mechanism,<sup>[29]</sup> a spontaneous phase separation process occurring in thermodynamically unstable regions. Based on the diffraction characteristics of the A2 and B2 phases,<sup>[14]</sup> their corresponding XRD peak positions are identified, as shown in Figure 1c. Furthermore, TEM-energy-dispersive X-ray spectroscopy (EDS) mapping reveals compositional differences between the two phases (Figure 1g). Specifically, the A2 phase is enriched in Co, Cr, and Fe, while the B2 phase is enriched in Al, Co, and Ni. The ordered B2 BCC phase exhibits Al-centered site ordering with transition metals at the corners, while the disordered A2 BCC phase features a random distribution of all elements across lattice sites.

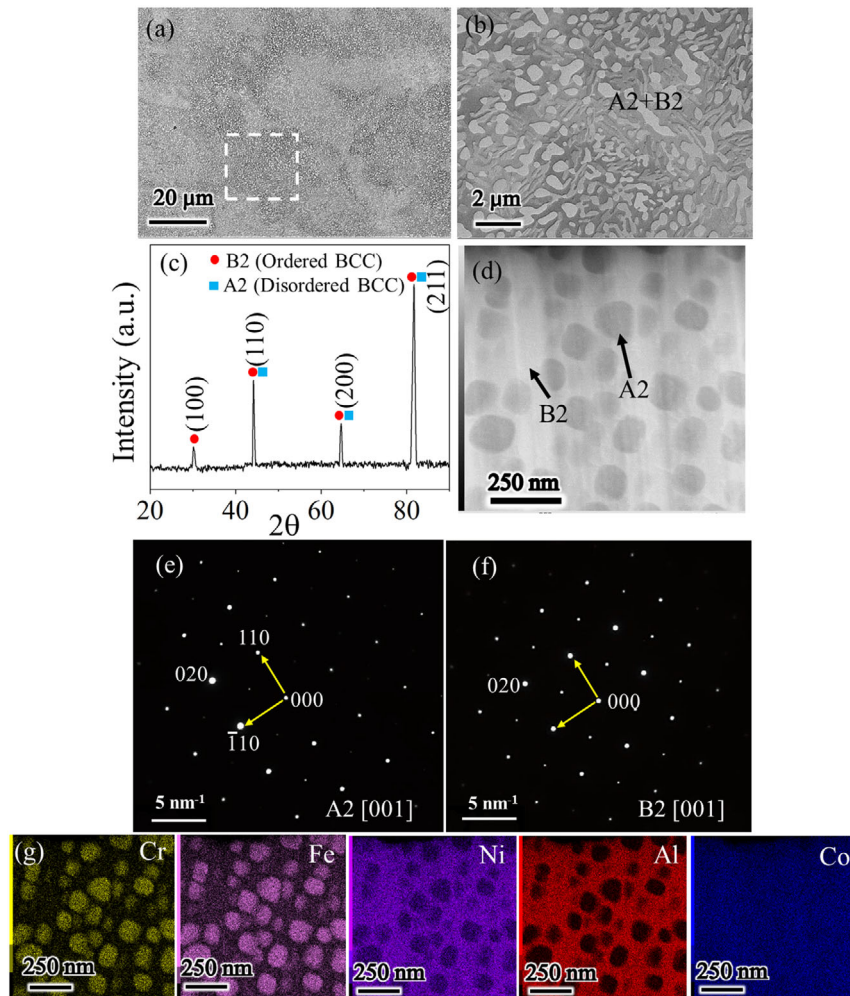


**Figure 1.** Microstructure and chemical composition distribution of the as-cast AlCoCrFeNi HEA: a,b) SE images at different magnifications; c) XRD pattern of the HEA; d) the microstructure of bright-field TEM image; e,f) SAED patterns along the<sup>[1]</sup> zone axis for the A2 and B2 regions, respectively; g) elemental distribution maps of Cr, Fe, Ni, Al, and Co.

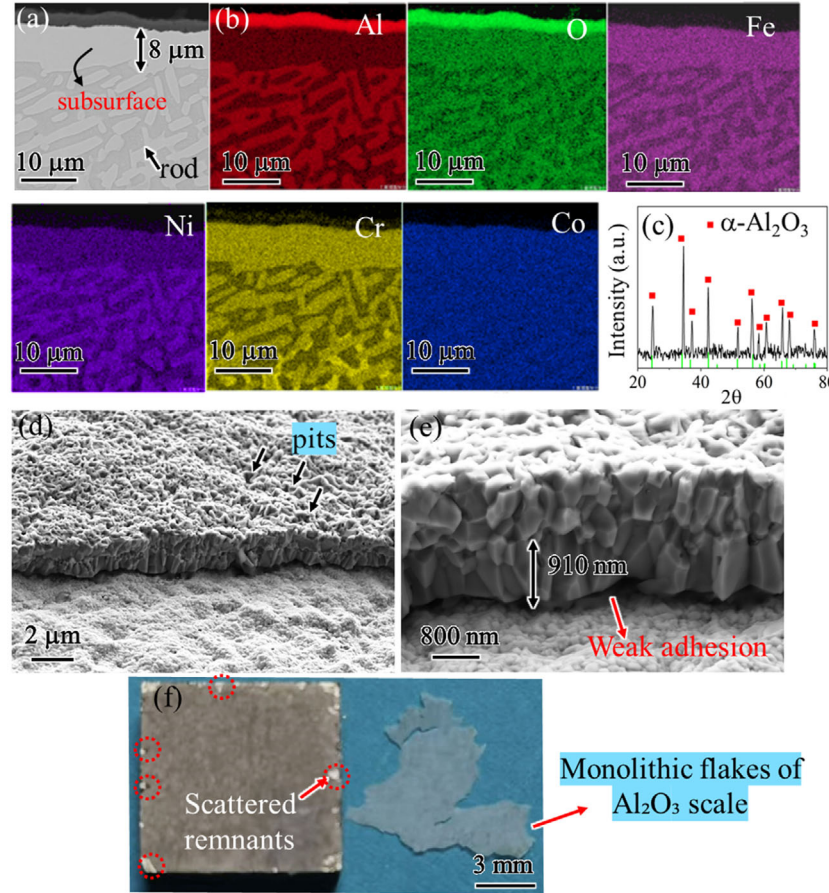
## 2.2. Microstructure of Oxide Scale and Subsurface AlCoCrFeNi HEA after Oxidation

Figure 2a,b display the cross-sectional microstructure and chemical composition distribution of the AlCoCrFeNi HEA after 50 h of oxidation at 1000 °C. The surface of HEA is covered by an oxide scale ≈1.5 μm thick. EDS analysis indicates that this oxide scale is primarily composed of Al and O, with no detectable traces of other HEA elements (Figure 2b). Moreover, XRD patterns confirm that the oxide scale is composed of Al<sub>2</sub>O<sub>3</sub> (Figure 2c). Beneath the oxide scale, a continuous Al-depletion layer (subsurface) ≈8 μm thick is observed within the subsurface region of the AlCoCrFeNi HEA (Figure 2a). EDS mapping results show that this subsurface layer is significantly depleted in Al and Ni, while enriched in Fe and Cr (Figure 2b). Additionally, beneath the subsurface region, the white precipitate-like areas observed in the as-cast specimens undergo a transformation, evolving into elongated, rod-like structures.

Figure 2d,e show the surface and fractured morphologies of the Al<sub>2</sub>O<sub>3</sub> scale after 50 h of oxidation at 1000 °C. The surface of

the Al<sub>2</sub>O<sub>3</sub> scale exhibits slight undulations along with numerous small pits, as shown in Figure 2d. The fractured cross-section, presented in Figure 2e, reveals that the Al<sub>2</sub>O<sub>3</sub> scale has a bilayer structure with nearly equal thickness (≈900 nm each). The upper layer is composed of equiaxed grains ≈350 nm in size, while the lower layer consists of columnar grains. Notably, the interface between the Al<sub>2</sub>O<sub>3</sub> scale and the AlCoCrFeNi HEA shows weak adhesion. This poor interfacial bonding results in the detachment of large, monolithic flakes of the Al<sub>2</sub>O<sub>3</sub> scale from the HEA surface. Only scattered remnants of the scale leave near the edges of the alloy (Figure 2f). This observation underscores the weak interfacial adhesion between the Al<sub>2</sub>O<sub>3</sub> scale and AlCoCrFeNi HEA.

Figure 3 illustrate the cross-sectional microstructure of the AlCoCrFeNi HEA and the fractured morphologies of the Al<sub>2</sub>O<sub>3</sub> scale after 200 h of oxidation at 1000 °C. The observations after 200 h of oxidation are broadly consistent with those recorded after 50 h. However, four significant differences are identified between the two oxidation durations: 1) The



**Figure 2.** The AlCoCrFeNi HEA after 50 h of oxidation at 1000 °C: a) cross-sectional microstructure; b) chemical composition distribution; c) XRD pattern of the oxide scale; d,e) surface and fractured morphologies of the  $\text{Al}_2\text{O}_3$  scale; f) macroscopic photographs of HEA and monolithic flakes of the  $\text{Al}_2\text{O}_3$  scale after 50 h oxidation.

Al-depletion layer (subsurface) expands substantially, reaching a width of 32  $\mu\text{m}$  (Figure 3a), driven by the continuous depletion of Al (Figure 3b); 2) The thickness of the equiaxed-grain  $\text{Al}_2\text{O}_3$  scale increases to 3  $\mu\text{m}$ , while that of the columnar-grain  $\text{Al}_2\text{O}_3$  scale grows to 5.4  $\mu\text{m}$  (Figure 3c,d); 3) Numerous nanopores develop within the equiaxed-grain  $\text{Al}_2\text{O}_3$  scale (Figure 3d). 4) A significant interfacial crack develops between the  $\text{Al}_2\text{O}_3$  scale and the AlCoCrFeNi HEA after 200 h of oxidation, as shown in Figure 3c. This interfacial crack prevents the white,  $\text{Al}_2\text{O}_3$  scale flakes from adhering completely and spontaneously to the oxidized HEA surface.

Figure 4 presents the oxidation kinetics curves of the AlCoCrFeNi HEA during oxidation at 1000 °C for 200 h. Oxidation kinetics is a crucial parameter for understanding the oxidation mechanisms of alloys. In the initial oxidation stage (within the first 30 h), the oxidation behavior is likely controlled by chemical reactions occurring directly at the surface. In the subsequent stage, a fully formed and dense oxide scale develops, which significantly slows down further oxidation of the substrate. At this stage, the oxidation process is governed by the diffusion of elements through the oxide scale rather than by surface of HEA chemical reactions. Consequently, the oxidation mass gain rate decreases over time due to the growth of the oxide scale. This

element-diffusion-controlled oxidation behavior follows a parabolic rate law, consistent with the classical Wagner oxidation theory ( $\Delta W = k_p t^{1/2}$ ).<sup>[30]</sup> The parabolic rate constant ( $k_p$ ) for the AlCoCrFeNi HEA is determined to be  $1.6 \times 10^{-5} \text{ mg cm}^2 \text{ s}^{-1}$ .

To further investigate the structure of the Al-depleted layer (subsurface), TEM analysis is performed, as illustrated in Figure 5. The EDS mapping results indicate a uniform distribution of Fe, Co, Ni, Cr, and Al, with no evidence of elemental segregation (Figure 5d). Moreover, the SAED patterns (highlighted within the white dotted circle in Figure 5c) confirm that the subsurface exhibits a face-centered cubic (FCC) structure, suggesting that the subsurface layer of the oxidized AlCoCrFeNi HEA consists entirely of FCC phases.

### 2.3. Effect of High Temperature on AlCoCrFeNi HEA Microstructure

Figure 6 illustrates the phase constitution, microstructure, and elemental distribution of the AlCoCrFeNi HEA after oxidation at 1000 °C for 200 h. The XRD result (Figure 6c) reveals that the phase constitution of the AlCoCrFeNi HEA comprises FCC, A2, and B2 phases after high-temperature oxidation. Notably, compared to the as-cast AlCoCrFeNi HEA, a new

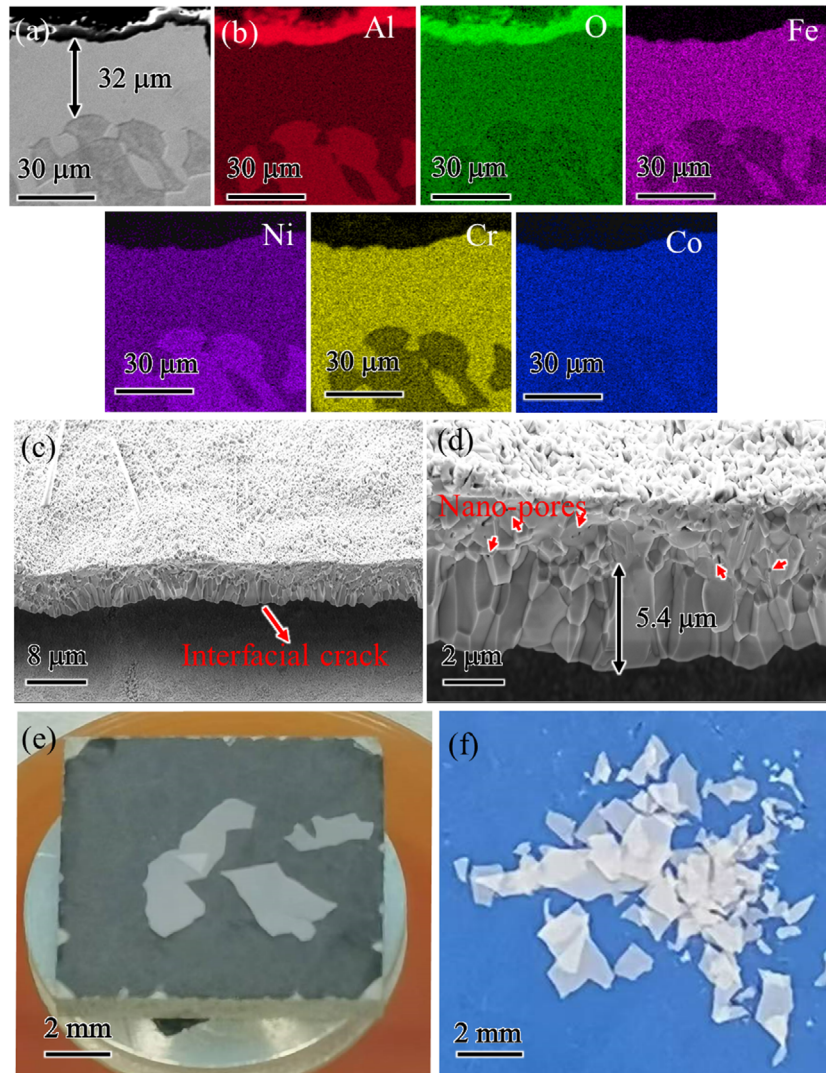


**Figure 3.** The AlCoCrFeNi alloy after 200 h of oxidation at 1000 °C: a) the cross-sectional microstructure and b) chemical composition distribution; c,d) the surface and fractured morphologies of the  $\text{Al}_2\text{O}_3$  scale; e,f) macroscopic photographs of HEA and monolithic flakes of the  $\text{Al}_2\text{O}_3$  scale after 200 h oxidation, respectively.

FCC phase is formed in HEA after high-temperature oxidation at 1000 °C. Meanwhile, the microstructural analysis (Figure 6a) shows that the most prominent feature of the alloy after high-temperature oxidation is the formation of a new phase  $\approx 5 \mu\text{m}$  wide along the grain boundary regions. This newly formed phase is identified as having an FCC structure, as confirmed by the SAED pattern obtained from the [AS011] FCC zone axis (Figures 6d–e). The EDS mappings analysis (Figure 6b) further demonstrates that the grain boundary regions are significantly depleted in Al and Ni, while being enriched in Fe and Cr. The elemental distribution in this phase transformation regions (grain boundary regions) closely resembles the characteristics of Al-depleted zones. Table 1 provides the atomic percentages of Fe, Co, Ni, Cr, and Al at multiple sampling points within the phase transformation regions.<sup>[31]</sup> As shown in the Table 1, the Al content in the subsurface layer and phase transformation

regions ranges between 5 and 7 at%. This reduction in Al content weakens lattice distortion within the high-entropy solid solution, increases the valence electron concentration, and reduces the electronegativity difference.<sup>[32]</sup> These factors collectively promote the phase transformation of the HEA structure from BCC to FCC. Consequently, the phases in the grain boundary regions and subsurface layer are identified as FCC. Moreover, no significant elemental segregation is also observed during this phase transformation regions, as shown in Figure 6g.

#### 2.4. Mechanical Properties of Specific Areas

Understanding the mechanical response of this region is essential, as oxidation-induced compositional and structural changes can significantly reduce its load-bearing capability and

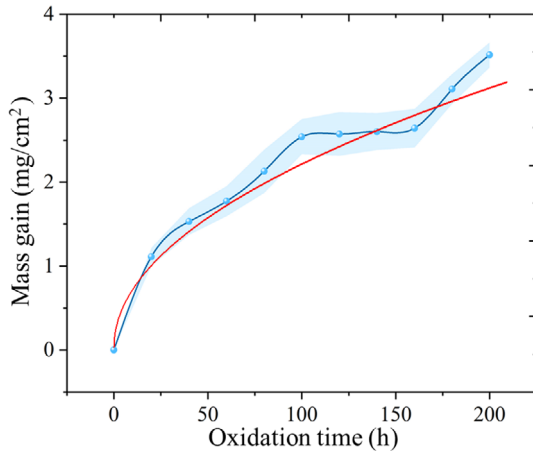


**Figure 4.** Oxidation kinetics curve of the AlCoCrFeNi HEA at 1000 °C for 200 h, the red line represents parabolic fitting based on Wagner's oxidation theory.

compromise the alloy's high-temperature durability. Here, in situ compression tests are performed on prepared nanopillars inside an scanning electron microscope (SEM). Fifty experimental pillar samples from the subsurface layer and phase transformation region of the AlCoCrFeNi HEA are analyzed. **Figure 7** presents the representative compressive stress-strain curves for mechanical pillar test in subsurface layer. During compression, the nanopillars initially undergo linear elastic deformation, followed plastic yielding, and eventually reach a stable plastic flow stage. In the plastic regime, discrete strain bursts and stress drops frequently occur. Each of these events corresponds to the intermittent nucleation of dislocations and subsequent slip activity during plastic deformation. These observations align with findings from prior studies on the in situ compression of single-crystalline FCC metallic nanopillars.<sup>[33]</sup>

To better distinguish the mechanical property differences between the subsurface layer and phase transformation region while minimizing the influence of crystal orientation and grain boundaries, the cumulative distribution function method is

adopted to statistically compare the yield strength of these two regions.<sup>[34]</sup> **Figure 8** shows the cumulative distributions of experimentally measured yield strength for the subsurface and phase transformation regions. As shown in the figure, the subsurface has a significantly lower average yield strength ( $\approx$ 1000 MPa) compared to the phase transformation region ( $\approx$ 1300 MPa). This indicates that even though both regions share an FCC structure and exhibit minimal differences in elemental composition, the subsurface layer demonstrates inferior mechanical performance compared to the phase transformation region.

Since this study focuses on the mechanical properties of the subsurface layer, only the deformation images of subsurface nanopillars are presented. **Figure 9a–c** present sequential snapshots of the plastic deformation process for subsurface region nanopillars under compression, with orientations of <100>, <110>, and <111>, respectively. These snapshots are captured during in situ SEM compression experiments. For <100>-oriented nanopillars, at the initial stage of plastic deformation, two slip traces form on different planes at the free surface (Figure 9a). As the strain increases, no additional slip planes are activated. This behavior is attributed to the Schmid factor of the leading partial dislocation (0.47), which is higher than that of the full dislocation (0.40) and the secondary partial dislocation (0.236).<sup>[35]</sup> This indicates that once the leading partial dislocation is activated and begins to glide, it does not favor activation of the trailing partial dislocation. For <110>-oriented nanopillars, two nonparallel slip traces appear on the free surface (Figure 9b), indicating the occurrence of double slip. With increasing strain, new dislocations are activated, gliding across the interior of the nanopillar and eventually escaping from the free surface. This process leaves behind a few slip steps and two shear bands on the surface (Figure 9b). For <111>-oriented nanopillars, in the early stages, numerous dislocations are activated on parallel slip planes and begin to glide. This eventually leads to the formation of localized shear bands (Figure 9c). This behavior demonstrates that single slip is the dominant deformation mechanism during the compression of <111>-oriented nanopillars. In

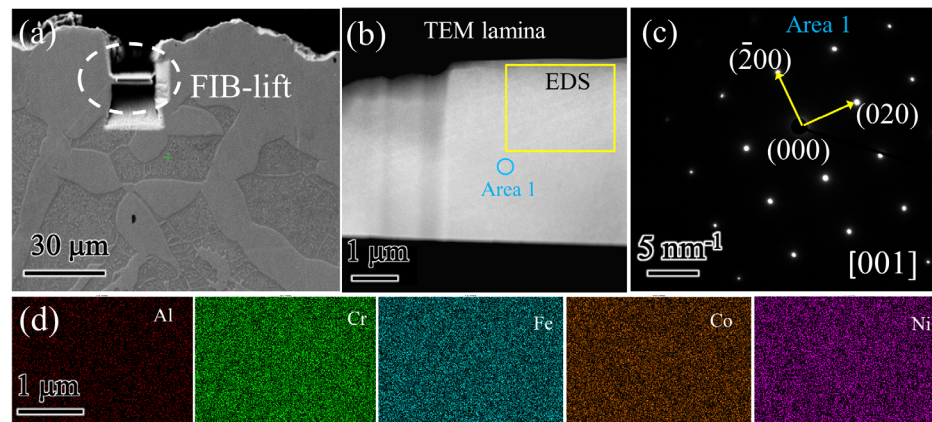


**Figure 5.** The subsurface layer of the oxidized AlCoCrFeNi HEA: a) thin lamellae of TEM prepared using FIB; b) bright-field TEM image showing the microstructure; c) SAED patterns of subsurface layer; and d) chemical composition distribution.

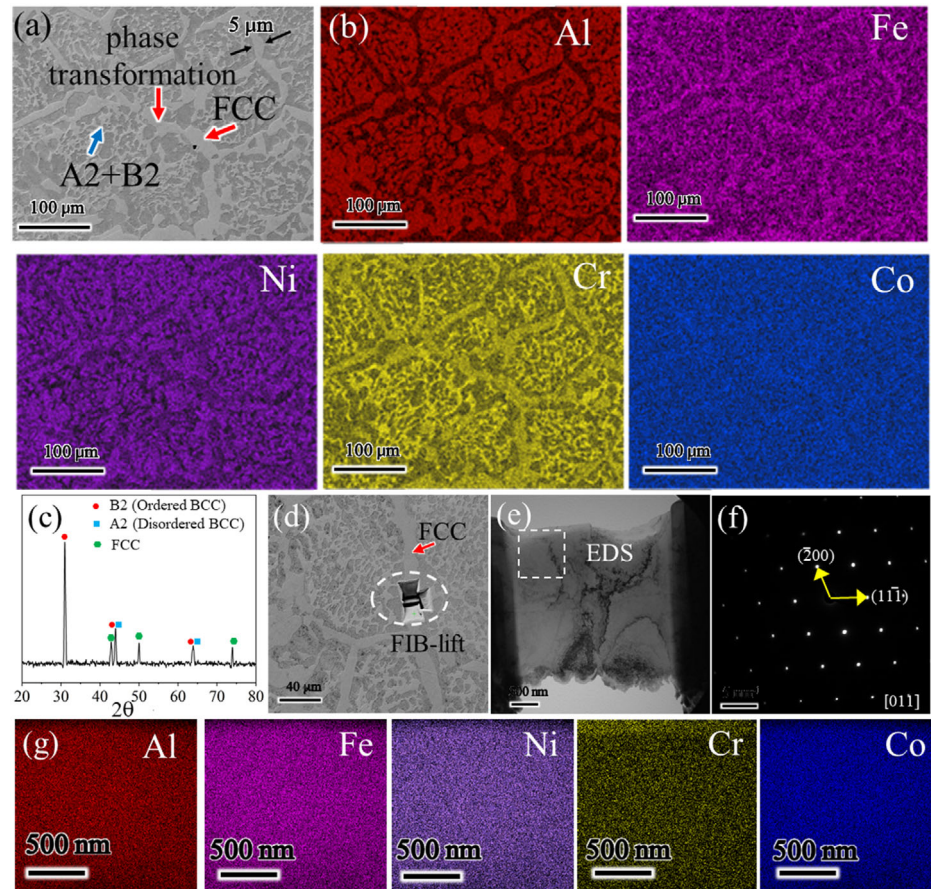


**Figure 6.** The AlCoCrFeNi HEA microstructure after high-temperature oxidation 200 h at 1000 °C: a) the core of microstructure for HEA; b) chemical composition distribution; c) XRD patterns; d) thin lamellae of TEM prepared using FIB in grain boundary regions; e) TEM image of grain boundary region; f and g) SAED pattern and EDS mappings of white dotted box in Figure 6e, respectively.

**Table 1.** The atomic percentages of Fe, Co, Ni, Cr, and Al at multiple sampling points in the grain boundary regions (phase transformation regions) and Al-depleted zones (subsurface layer).

at [%]	Al-depleted zones					Grain boundary regions				
	1#	2#	3#	4#	5#	1#	2#	3#	4#	5#
Fe	26.69	27.36	26.56	27.38	26.95	26.68	26.72	27.31	27.37	27.29
Co	28.32	27.78	28.15	27.65	28.41	27.38	26.95	26.93	26.67	26.27
Ni	15.16	15.00	14.53	15.94	15.10	15.64	15.89	15.92	15.95	15.94
Cr	24.29	24.05	25.14	23.64	23.80	23.36	23.64	23.16	23.21	23.49
Al	5.54	5.81	5.62	5.39	5.74	6.94	6.80	6.68	6.80	7.01

summary, the plastic deformation of subsurface nanopillars is predominantly governed by dislocation slip.

### 3. Discussion

#### 3.1. Growth Mechanism of Scale

In our experiment, the  $\text{Al}_2\text{O}_3$  scale consists of both equiaxed grains and columnar grains. The formation of these structures is closely related to the diffusion behavior of Al and O. When Al

ions diffuse along the grain boundaries of scale to the oxide surface, they react with O to form  $\text{Al}_2\text{O}_3$ . Due to the uniform distribution of the grain boundary network of scale, the diffusion path of Al ions exhibits high uniformity and weak directionality. Consequently, the growth of  $\text{Al}_2\text{O}_3$  on the surface occurs isotropically, leading to the formation of equiaxed grains with random orientation. The weak directionality of equiaxed grain growth and the random distribution of grains result in relatively large grain boundary gaps, leading to porosity formation in this region (Figure 3d). This phenomenon is

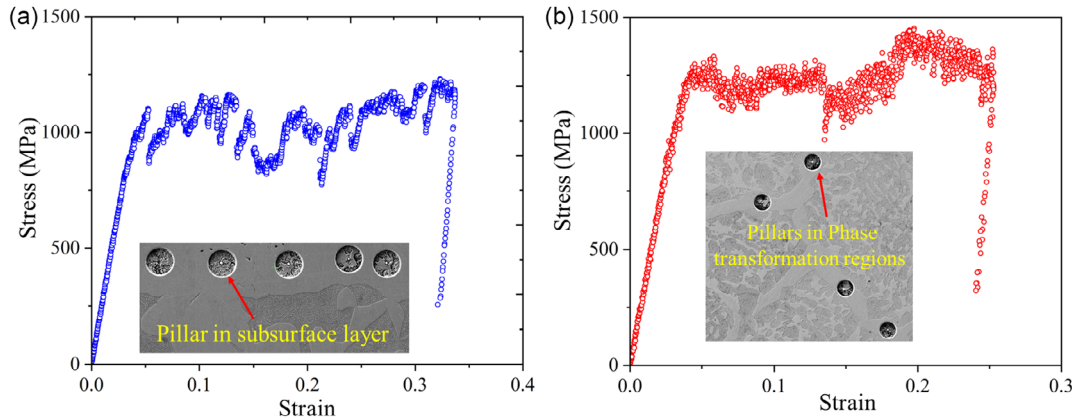


**Figure 7.** The representative compressive stress-strain curves for pillar in a) subsurface layer and b) phase transformation region.

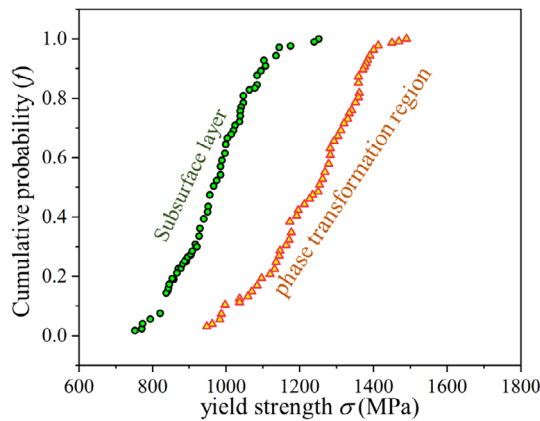


**Figure 8.** The cumulative distribution of yield strengths for subsurface and phase transformation region.

more pronounced during the early stages of oxidation. As shown in **Figure 10**, which presents the interfacial structure of the oxide scale after 20 h of oxidation, the majority of the oxide layer is composed of equiaxed grains. This supports our conclusion that equiaxed-grain-dominated growth and its associated porosity is a characteristic feature of the early oxidation stage.

With the increase in oxidation time, the formation of columnar grains in  $\text{Al}_2\text{O}_3$  is primarily driven by the inward diffusion of O. Oxygen diffuses along the grain boundaries of the  $\text{Al}_2\text{O}_3$  scale to the interface between the oxide layer and the surface of HEA, where oxygen react with Al to form new  $\text{Al}_2\text{O}_3$ . The growth of  $\text{Al}_2\text{O}_3$  is concentrated near the substrate interface, propagating inward along the grain boundaries and forming a structure perpendicular to the surface, which results in columnar grains. Experimental results show that with increasing oxidation time, the thickness of both the columnar and equiaxed grains in the  $\text{Al}_2\text{O}_3$  layer increases (**Figure 2, 3**). This indicates that the outward diffusion of Al and the inward diffusion of O occur simultaneously. However, the thickness of the columnar grains is greater than that of the equiaxed grains (**Figure 3**), which suggests that the inward diffusion rate of O is higher than the

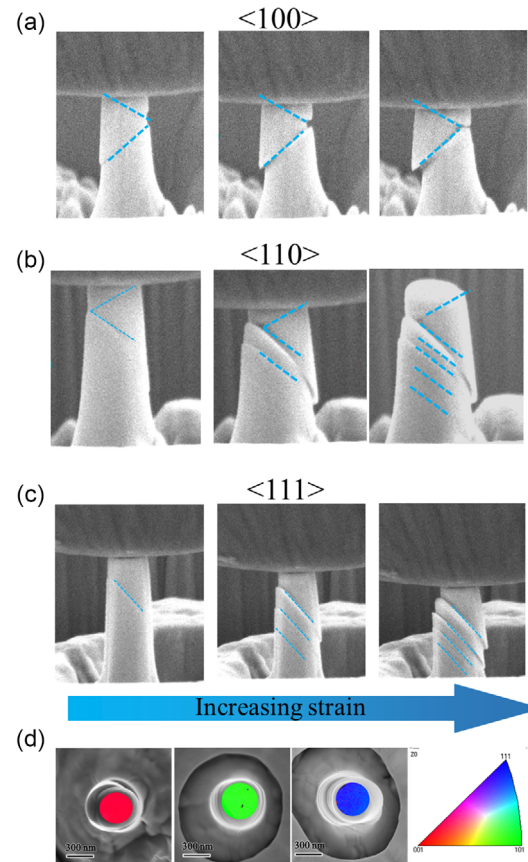


**Figure 9.** A sequence of snapshots of HEA pillars with an orientation of a)  $<100>$ , b)  $<110>$ , and c)  $<111>$  during in situ compression, the dashed lines indicating the plastic events during yielding; d) the top view and surface crystal orientation of compressed pillar.

outward diffusion rate of Al. The schematic illustration showing diffusion of Al and O in scale and interface is shown in **Figure 11**.

The formation of a bilayer  $\text{Al}_2\text{O}_3$  structure has been observed during the oxidation of alloys doped with reactive elements (e.g., Y, Zr, and Hf).<sup>[36–39]</sup> These reactive elements suppress the diffusion of Al. By suppressing the outward diffusion of Al, reactive

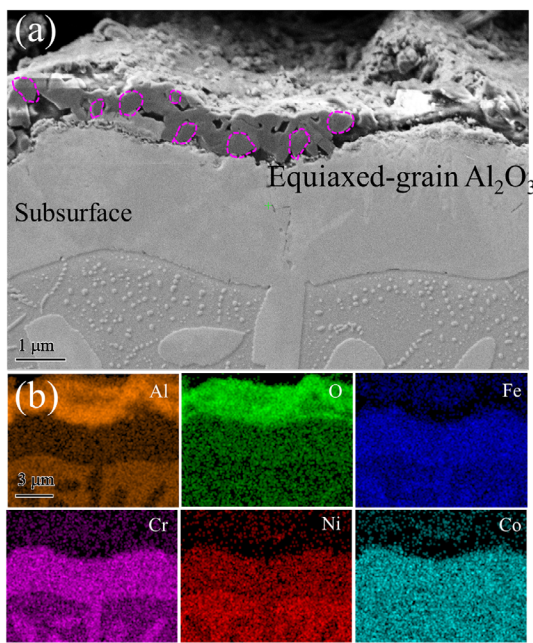


**Figure 10.** The AlCoCrFeNi alloy after 20 h of oxidation at 1000 °C: a) the cross-sectional microstructure and b) chemical composition distribution.

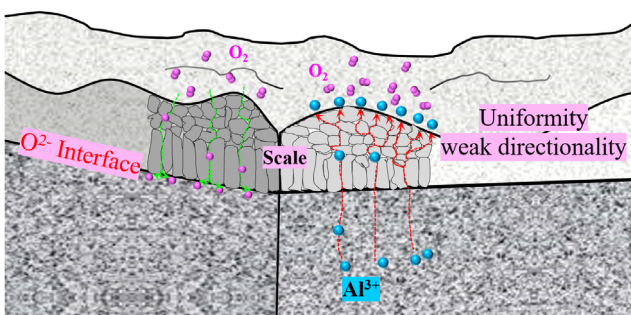


**Figure 11.** The schematic illustration showing diffusion behavior of Al and O in scale and interface.

elements shift the diffusion balance in favor of inward oxygen transport. This oxygen-dominated oxidation mechanism facilitates the preferential growth of columnar grains at the alloy/oxide interface. However, since the AlCoCrFeNi HEA does not contain reactive elements, the bilayer structure must be attributed to the diffusion coefficient of Al ( $D_{Al}$ ) in the subsurface FCC structure. To investigate this, we calculate  $D_{Al}$  in both the subsurface FCC and BCC substrates structure (in equiatomic ratios) by the mean square displacement (MSD).  $D_{Al}$  is determined from the slope of the MSD versus time ( $t$ ) plot, as expressed by the following equation<sup>[40]</sup>

$$MSD = 6D_{Al} \cdot t \quad (1)$$

**Figure 12** show the MSD calculated using MD simulations for the subsurface FCC and BCC substrate structures. Clearly,  $D_{Al}$  in the subsurface FCC structure ( $1.8 \times 10^{-11} \text{ m}^2 \text{ s}^{-1}$ ) is lower than

that in the BCC substrate structure ( $4.17 \times 10^{-11} \text{ m}^2 \text{ s}^{-1}$ ). Thus, the phase transformation in the subsurface layer acts as an additional effect that further enhances the oxidation resistance of the HEA. This trend is systematically reinforced by the dual-phase polycrystal structures results: the  $D_{Al}$  increases progressively with higher BCC phase fraction (Figure 11c), yielding values of  $4.9 \times 10^{-10}$ ,  $5.3 \times 10^{-10}$ ,  $6.3 \times 10^{-10}$ , and  $7.3 \times 10^{-10}$  for FCC-to-BCC grain number ratios of 6:0, 4:2, 2:4, and 0:6, respectively. These results demonstrate that Al diffusion accelerates as the BCC phase fraction increases. It is worth noting that the Al diffusion coefficient in polycrystalline systems is typically one order of magnitude higher than that in single crystals. This is consistent with expectations, as grain boundaries serve as fast diffusion pathways for Al atoms.

### 3.2. Vacancy Formation and its Induced Low Interface Adhesion Behavior

The experimental results reveal that the oxide scale formed on AlCoCrFeNi HEA adheres poorly to the HEA, often resulting in large-scale spallation (Figure 2 and 3). While this detachment is commonly attributed to growth stresses and thermal mismatch stresses, another critical contributing factor is the direct effect of injected interface vacancies.<sup>[41]</sup>

Here, we focus on analyzing the impact of vacancies on the adhesion ability of the oxide scale. During the initial stages of oxidation, Al ions diffuse outward from the surface layer of HEA, leading to the formation of metal vacancies at the oxide scale/HEA interface.<sup>[24]</sup> Many of these vacancies are not annihilated but instead coalesce to form vacancy clusters. These vacancy clusters give rise to low-density regions and voids near the surface of the HEA, further weakening the adhesion between the oxide scale and HEA. The low-density regions and voids can be directly linked to the intermediate contrast regions observed in scanning transmission electron microscopy (STEM) image, as shown in **Figure 13**. This structural degradation significantly compromises the scale's ability to remain attached to the HEA surface.

During the middle and late stages of oxidation, the selective oxidation of Al ion not only drives an Al flux ( $J_{Al}$ ) toward the oxide scale/HEA interface but also induces a redistribution of other elements in the alloy. Here, the fastest diffusing element in the alloy is Ni, with its self-diffusion rate being three times that of Al at 1000 °C.<sup>[42]</sup> This leads to the formation of a symmetric nickel concentration profile, with the corresponding nickel flux ( $J_{Ni}$ ) directed inward, towards the core of the HEA. Due to the mismatch between the intrinsic diffusion coefficients of the alloy's constituents, an imbalance arises between the material fluxes.<sup>[43]</sup> To restore flux equilibrium, a vacancies flux ( $J_V$ ) is generated, moving in the opposite direction to the fastest diffusing element. This process is commonly referred to as the Kirkendall effect<sup>[44]</sup> and the schematic diagram is shown in **Figure 14a**.

As a result, vacancies diffuse toward the oxide scale/HEA interface, following the relationship  $|J_V| = |J_{Al} - J_{Ni}|$ . Consequently, throughout the oxidation process, the interface acts as a sink for vacancies, leading to significant vacancy coalescence.<sup>[41]</sup> With the accumulation of vacancies at the interface, voids eventually form. These voids increase the contact

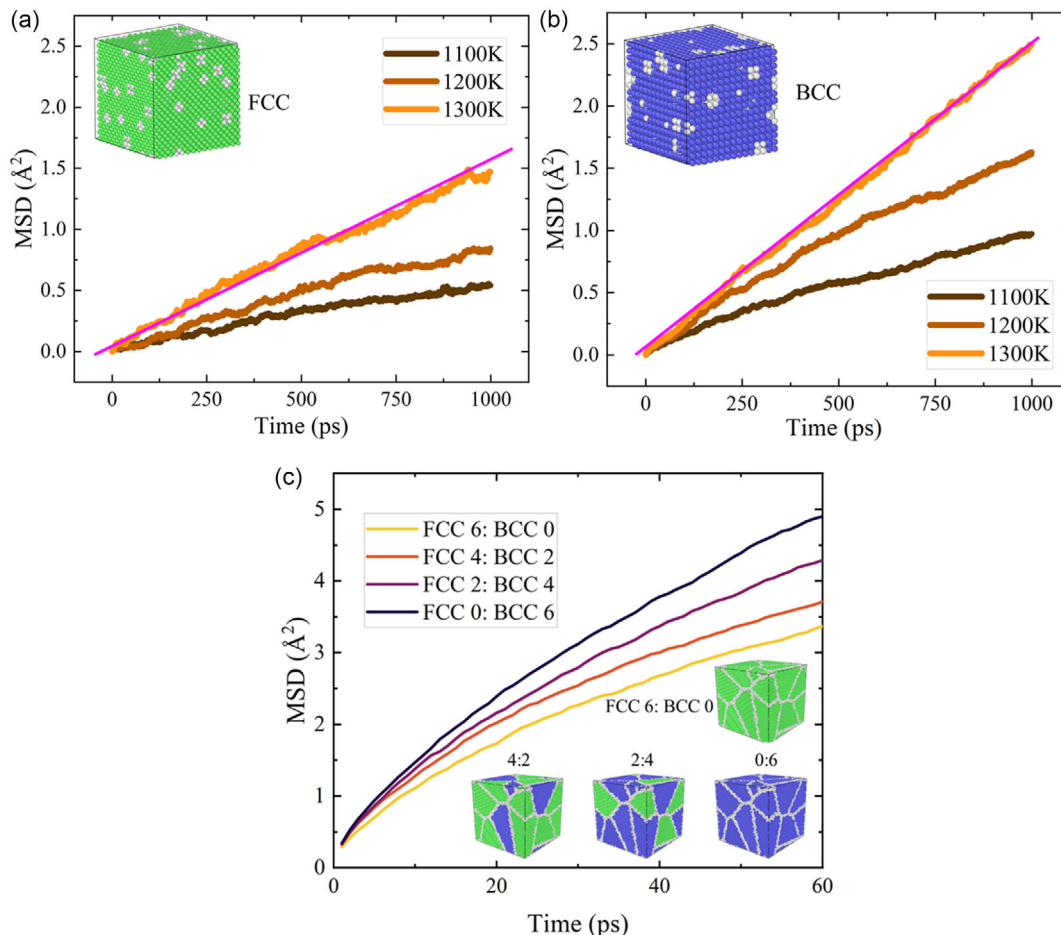


**Figure 12.** MD simulations of atomic migration behavior (MSD of Al) in a) subsurface layer, b) substrate structure, and c) dual-phase polycrystals structure.

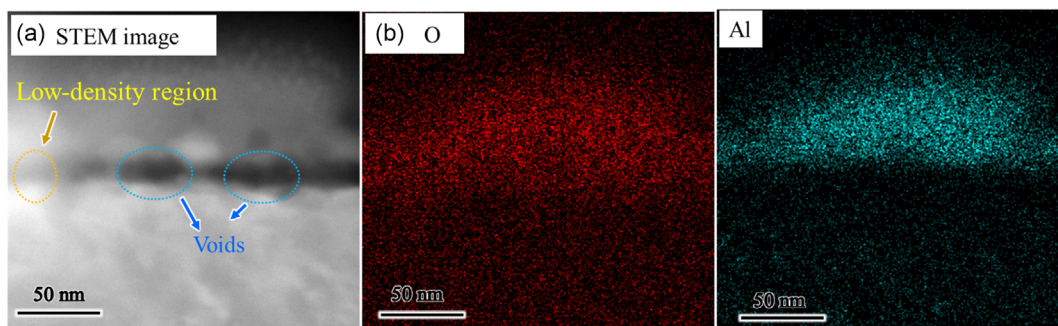


**Figure 13.** The low-density regions and voids at the interface of the AlCoCrFeNi HEA after only 120 s of oxidation: a) STEM and b) EDS mapping of O and Al.

angle ( $\theta$ ) between the HEA surface and the oxide scale (as shown in Figure 14b). Generally, the pores are shallow, with an average diameter ( $d$ ) at least five times larger than their depth ( $h$ ), as shown in Figure 15. This high width-to-depth ratio remains consistent even at grain boundaries, where vacancies preferentially coalesce (Figure 15c). Meanwhile, the energy balance for this process can be expressed as<sup>[41]</sup>

$$\gamma_{if} = \gamma_{metal} \cdot \cos(\pi - \theta) + \gamma_{oxide} \quad (2)$$

where  $\gamma_{metal}$  and  $\gamma_{oxide}$  are intrinsic surface energy of the metal surface and oxide, respectively. Due to the obtuse contact angle ( $\theta$ ), the interfacial energy ( $\gamma_{if}$ ) is relatively low. As a result, the adhesion between the oxide scale and the metal is poor.

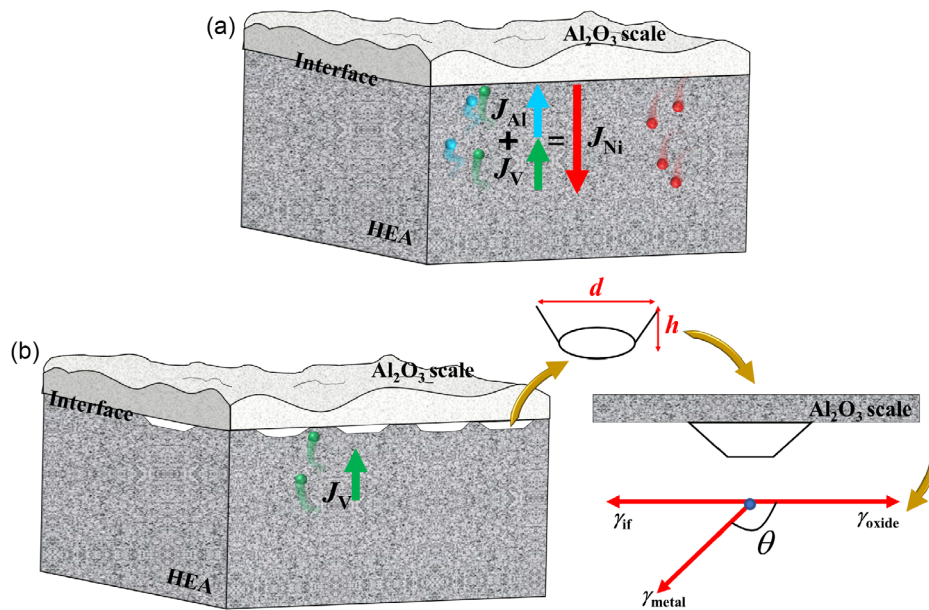


**Figure 14.** a) The schematic diagram of Kirkendall effect and b) schematic illustration showing pore morphology and the energy balance at pore edge.

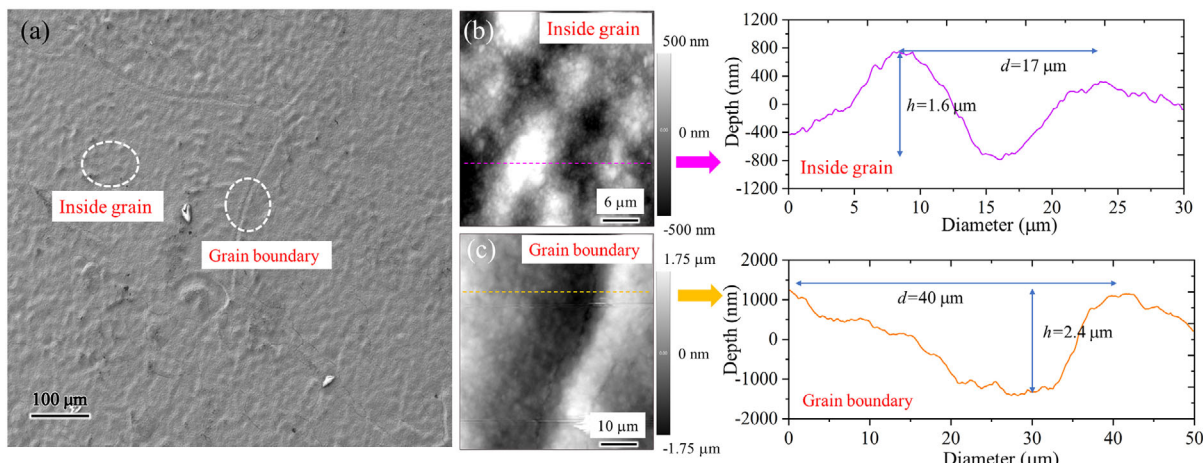


**Figure 15.** a) SEM images of the HEA surface morphology after oxide scale spallation; b) and c) AFM measurements of the surface roughness within grains and grain boundary, respectively.

### 3.3. Degradation Behavior of Subsurface of FCC

Generally, for solid solutions, higher Al content is associated with lower yield strength in alloy systems.<sup>[45]</sup> To verify whether this conclusion also holds true for the FCC AlCoCrFeNi HEA system, MD simulations are performed. Figure 16 presents the stress-strain curves for FCC AlCoCrFeNi HEA nanopillars with varying Al content under compression. Clearly, the yield strength of the HEA decreases as the Al content increases. Interestingly, for the FCC system, the subsurface layer with lower Al content (average  $\approx 5.5\%$ ) has a slightly lower yield strength than the phase transformation region (average  $\approx 6.7\%$ ). This experimental observation contradicts the MD simulation results. This also suggests that, in addition to the

influence of Al content, other factors also play a role in determining the yield strength of the subsurface layer.

As described in Section 4.2, high-temperature oxidation of AlCoCrFeNi HEAs introduces vacancies into the core of the HEA. Although some of these vacancies diffuse from the subsurface layer to the oxide scale/HEA interface, a portion remains within the subsurface layer without being eliminated.<sup>[46]</sup> This phenomenon has also been observed in oxidation experiments on Ni metal.<sup>[46]</sup> Therefore, when studying the yield strength of the subsurface layer, the influence of vacancies, in addition to the Al-depletion, must be considered. From the microstructural images of the subsurface layer, no voids are observed (Figure 2 and 3), indicating that the vacancy concentration in the subsurface alloy does not reach supersaturation. The Al content

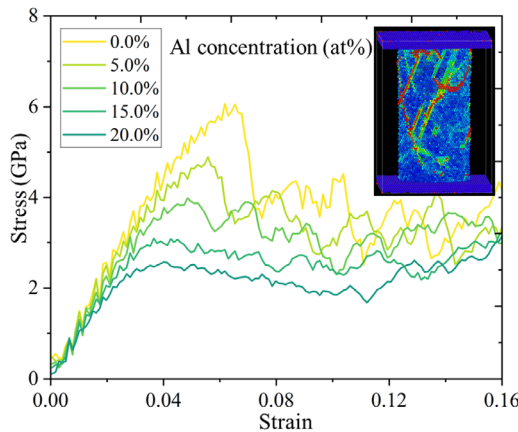


**Figure 16.** The strain-stress curves for FCC AlCoCrFeNi HEA nanopillars with varying Al content under MD compression simulation.

difference between the phase transformation region and the subsurface layer is  $\approx 1\%$ . However, this does not imply that the vacancy concentration in the subsurface layer is 1%, as a significant number of vacancies are annihilated at interfaces, grain boundaries, and dislocations during high-temperature oxidation. As a result, it is challenging to precisely determine the vacancy concentration in the subsurface layer. Here, to investigate the influence of vacancy concentration on yield strength and stacking fault energy (SFE) in FCC AlCoCrFeNi HEA, in order to interpret the mechanical softening observed experimentally in the oxidized subsurface. We conducted MD simulations under varying vacancy concentrations to study the impact of vacancies on the yield stress of HEAs. **Figure 17a–c** present the stress-strain curves of subsurface layer nanopillars under compression at different vacancy concentrations (0–0.04). The results show that, for HEA with different crystallographic orientations, the yield stress decreases as the vacancy concentration increases (**Figure 17d**).

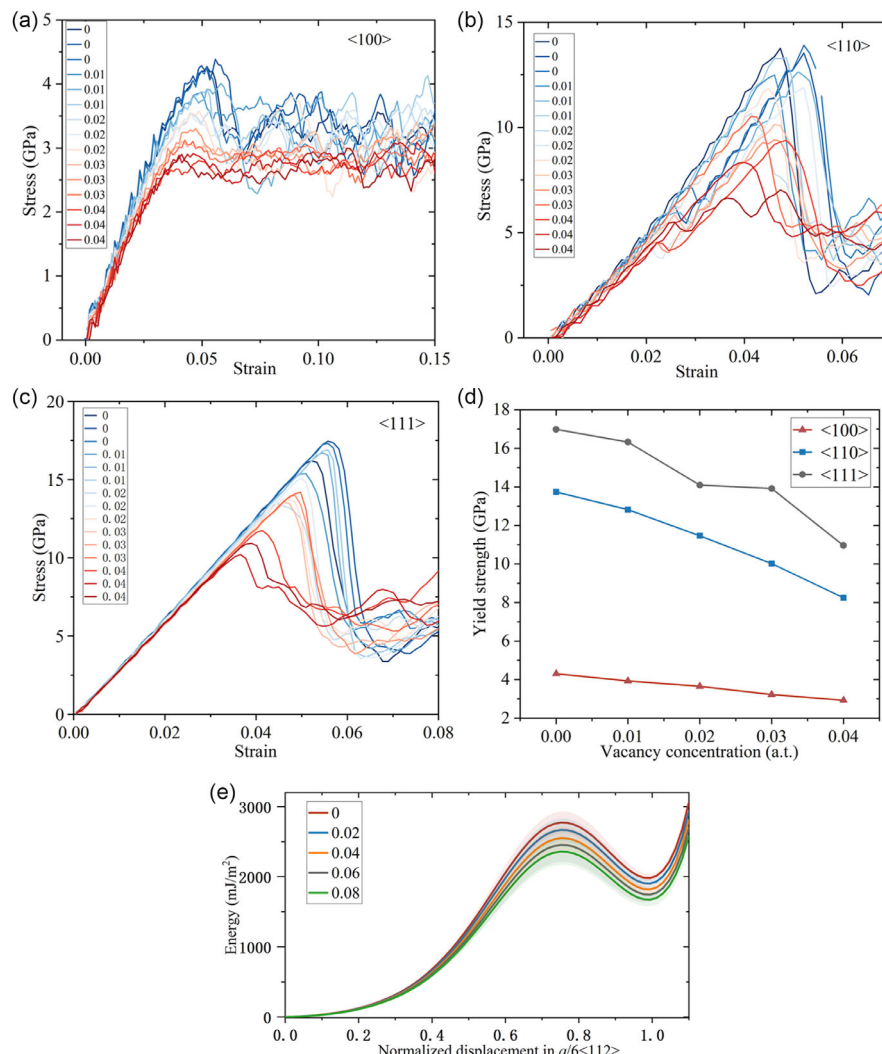


**Figure 17.** The stress-strain curves of subsurface layer nanopillars under compression at different vacancy concentrations: a)  $<100>$ -orientation; b)  $<110>$ -orientation; c)  $<111>$ -orientation; d) yield strengths versus vacancy concentrations; and e) SFE of the HEA versus vacancy concentrations.

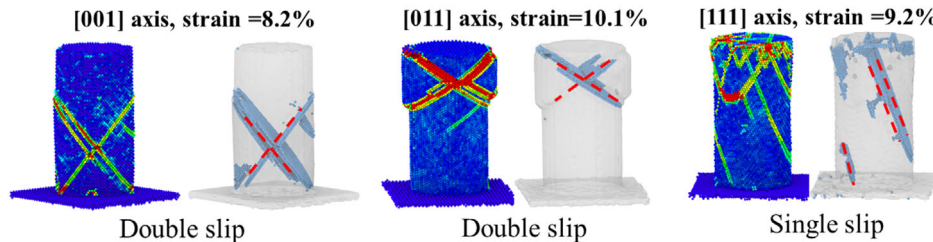


**Figure 18.** The simulated deformation behaviors of  $<100>$ ,  $<110>$ , and  $<111>$  orientations nanopillar under compression.

This is primarily because vacancies reduce the SFE of the HEA (Figure 17e), facilitating plastic deformation.

Furthermore, lower SFE increases the likelihood of dislocation avalanches, which explains the more frequent strain bursts observed during the plastic flow stage of subsurface alloys in Figure 7, compared to the deformation behavior of alloys in the phase transformation region. In addition, the simulated deformation behaviors (Figure 18) are generally consistent with the experimental results (Figure 8). Specifically, HEA pillars with  $<100>$  and  $<110>$  orientations primarily exhibit double slip, while those with a  $<111>$  orientation also primarily exhibit double slip.

#### 4. Conclusion

This study investigates the oxidation behavior and subsurface mechanical degradation of AlCoCrFeNi HEA at 1000 °C. The key findings are as follows: 1) High-temperature oxidation of AlCoCrFeNi HEA results in the formation of a bilayer  $\text{Al}_2\text{O}_3$  oxide scale, composed of equiaxed and columnar grains. Severe spallation occurs due to vacancy coalescence at the oxide/alloy interface, driven by outward Al diffusion and the Kirkendall effect. These vacancies form voids and low-density regions, significantly reducing interfacial adhesion and causing large oxide scale detachment. 2) Oxidation-induced Al depletion and BCC-to-FCC phase transformation in the subsurface layer enhance oxidation resistance by reducing  $D_{\text{Al}}$ . In addition, the mechanical property of subsurface exhibits  $\approx 30\%$  yield strength reduction due to vacancy formation and SFE reduction, which facilitate dislocation activity and plastic deformation. These findings underline the critical role of vacancy dynamics and subsurface phase stability in optimizing the high-temperature performance of HEAs for extreme environments.

#### 5. Experimental Section

**Alloy Preparation and Exposure Conditions:** The as-cast samples of AlCoCrFeNi HEA were prepared by vacuum arc melting high-purity elemental constituents ( $\geq 99.9$  wt%) on a water-cooled copper hearth using a large bell jar arc melting unit (ABJ-900, Materials Research Furnaces, Inc., USA). The melting was performed under a Ti-gettered high-purity argon atmosphere after evacuating the chamber to a base pressure below 0.01 Torr ( $\approx 1.3$  Pa). To ensure chemical homogeneity, each ingot was melted and solidified at least five times, flipping the sample between each cycle. After the arc melting, the ingot of AlCoCrFeNi HEA was sectioned into specimens with dimensions of  $10 \times 10 \times 2$  mm $^3$  using wire-electrode

cutting. Then, the surfaces of the specimens were prepared by sequential grinding with SiC sandpapers up to a P4000 grit size, followed by progressive polishing with an alumina suspension to achieve a surface roughness of  $\approx 50$  nm. Finally, vibratory polishing with corrosive  $\text{SiO}_2$  suspension was performed for 6 h to relieve residual surface stresses and enhance surface smoothness.

Three specimens were placed in alumina crucibles and subjected to isothermal oxidation in static air at 1000 °C using a muffle furnace. Both the heating and cooling rates were controlled at  $10\text{ }^{\circ}\text{C min}^{-1}$ . The mass of each crucible, including the specimen, was measured at various intervals before and after oxidation using a high-precision electronic balance (accuracy: 0.01 mg, Quintix65-1cN). Notably, the alumina crucibles were preheated at 1000 °C for a sufficient duration to stabilize their weights prior to the isothermal oxidation tests, ensuring that any observed mass change was solely due to the oxidation of the alloy.

**Characterizations:** The phase compositions of the AlCoCrFeNi HEA (before and after oxidation) and the oxide scales, were analyzed using XRD (XRD, D8 ADVANCE, Bruker AXS, Germany) with Cu K $\alpha$  radiation at 40 kV. The diffraction patterns were recorded over a  $2\theta$  range of  $10\text{--}90^\circ$  with a step size of  $0.02^\circ$ .

Surface morphology was examined in secondary electron (SE) imaging mode, and phase contrast is analyzed in back-scattered electron imaging mode using a SEM (SEM, Crossbeam 550, Zeiss, Germany). The electron backscatter diffraction (EBSD, Oxford Instruments) analysis was conducted in a SEM to characterize the orientation. Chemical composition was determined by EDS (EDS, Oxford Instruments). Thin lamellae, less than 80 nm in thickness, were prepared from the samples using a focused ion beam (FIB) (FIB, Crossbeam 550, Zeiss, Germany). These lamellae were further analyzed using a TEM (TEM, JEM-F200, JEOL, Japan) equipped with an EDS system (EDS, XIS Ultra DLD, Kratos, Japan). Surface roughness measurements were performed using atomic force microscopy (AFM) on an Asylum Research Cypher AFM system (Oxford Instruments).

Uniaxial compression samples with a diameter of 500 nm were fabricated using FIB milling (Crossbeam 550, Zeiss, Germany). The fabrication process involves applying concentric circular milling patterns via the FIB until a cylindrical pillar with an aspect ratio of 2.5:1 (height-to-diameter ratio) was achieved. The micropillar compression tests were performed after high-temperature oxidation (1000 °C for 200 h) to evaluate the oxidation-induced mechanical degradation in the subsurface layer, which serves as a critical crack initiation site during service. Compression tests were performed using a nanomechanical testing system (FT-NMT04, FemtoTools, Buchs, Switzerland) equipped with a 5  $\mu\text{m}$  diameter diamond flat punch. The experiments were conducted in displacement rate-controlled mode, while maintaining a constant displacement rate of  $10\text{ nm s}^{-1}$  throughout the testing process.

**MD Simulations:** Selecting a proper potential that is accurate in predicting atomic interactions among the multiple chemical species in HEA is crucial for reliable MD simulations. In this study, we employed a recently developed embedded atom method (EAM) potential for the Al/Co/Cr/Fe/Ni system. Detailed potential development and validation will be reported elsewhere. All simulations were performed using LAMMPS (version 9 Aug 2019)<sup>[47]</sup> with a timestep of 1.0 fs; atomic trajectories are visualized using OVITO software (version 4.6.0).<sup>[48]</sup>

To examine the effects of Al content and vacancy concentration on the mechanical properties of FCC AlCoCrFeNi HEA, defect-free single crystals with dimensions  $50a \times 50a \times 50a$  were constructed (where  $a = 3.616 \text{ \AA}$  is the stress-free lattice constant predicted by the EAM potential). Their Al content varies from 0% to 20%. Additionally, bulk crystals with compositions similar to those observed experimentally in subsurface and transformation regions (Fe: 26%, Co: 27%, Ni: 15%, Cr: 25% and Al: 7%) were created; vacancies were introduced by randomly removing metal atoms. These models were initially equilibrated at 300 K for 100 ps using an NPT ensemble to release internal stress. Nanopillars with a radius of 40 Å were cut from the thermally equilibrated bulk crystals and then uniaxially compressed at a typical MD strain rate of  $5 \times 10^8 \text{ s}^{-1}$ .<sup>[49]</sup> The corresponding stress variations and atomic structural evolutions were recorded and analyzed.

To compare the diffusion coefficients of aluminum in the multiphase HEA,  $15a \times 15a \times 15a$  supercells of FCC and BCC models were constructed with 3D periodic boundary conditions. The models were first heated to a specific temperature (i.e., 1100 K, 1200 K, and 1300 K) for 1.0 ns; an NPT ensemble was utilized to release thermal stress. Thereafter, the system was equilibrated at the target temperature for another 2.0 ns in an NVT ensemble. MSDs during equilibration are calculating to reveal atomic diffusion behaviors. The dual-phase polycrystal samples were constructed using the Voronoi construction method containing 6 grains with random crystallographic orientations, and the mean grain size was 5.5 nm.

## Acknowledgements

The authors would like to express the gratitude for the support of NSFC (grant nos: 12202341 and 12090030) and the 111 Project (B18040).

## Conflict of Interest

The authors declare no conflict of interest.

## Data Availability Statement

The data that support the findings of this study are available from the corresponding author upon reasonable request.

## Keywords

AlCoCrFeNi high-entropy alloys, mechanical degradations, oxide detachments, vacancies

Received: April 24, 2025

Revised: July 15, 2025

Published online:

- [1] E. P. George, D. Raabe, R. O. Ritchie, *Nat. Rev. Mater.* **2019**, 4, 515.
- [2] Y. Ye, Q. Wang, J. Lu, C. Liu, Y. Yang, *Mater. Today* **2016**, 19, 349.
- [3] D. B. Miracle, O. N. Senkov, *Acta Mater.* **2017**, 122, 448.
- [4] Q. Guo, H. Hou, Y. Pan, X. Pei, Z. Song, P. K. Liaw, Y. Zhao, *Mater. Des.* **2023**, 231, 112050.
- [5] W. Li, D. Xie, D. Li, Y. Zhang, Y. Gao, P. K. Liaw, *Prog. Mater. Sci.* **2021**, 118, 100777.
- [6] J. Chen, X. Zhou, W. Wang, B. Liu, Y. Lv, W. Yang, D. Xu, Y. Liu, *J. Alloys Compd.* **2018**, 760, 15.

- [7] Y. Qiu, S. Thomas, M. A. Gibson, H. L. Fraser, N. Birbilis, *NPJ Mater. Degrad.* **2017**, 1, 15.
- [8] P. Sharma, V. Dwivedi, S. P. Dwivedi, *Mater. Today: Proc.* **2021**, 43, 502.
- [9] E. Pickering, N. Jones, *Int. Mater. Rev.* **2016**, 61, 183.
- [10] Z. Lu, H. Wang, M. Chen, I. Baker, J. Yeh, C. Liu, T. Nieh, *Intermetallics* **2015**, 66, 67.
- [11] B. MacDonald, Z. Fu, B. Zheng, W. Chen, Y. Lin, F. Chen, L. Zhang, J. Ivanisenko, Y. Zhou, H. Hahn, *Jom* **2017**, 69, 2024.
- [12] M. Tokarewicz, M. Grądzka-Dahlke, *Metals* **2021**, 11, 1302.
- [13] K. R. Lim, K. S. Lee, J. S. Lee, J. Y. Kim, H. J. Chang, Y. S. Na, *J. Alloys Compd.* **2017**, 728, 1235.
- [14] J. Lu, L. Li, H. Zhang, Y. Chen, L. Luo, X. Zhao, F. Guo, P. Xiao, *Corros. Sci.* **2021**, 181, 109257.
- [15] Z. Tang, O. N. Senkov, C. M. Parish, C. Zhang, F. Zhang, L. J. Santodonato, G. Wang, G. Zhao, F. Yang, P. K. Liaw, *Mater. Sci. Eng.: A* **2015**, 647, 229.
- [16] T. M. Butler, M. L. Weaver, *J. Alloys Compd.* **2016**, 674, 229.
- [17] J. Zhu, S. Lu, Y. Jin, L. Xu, X. Xu, C. Yin, Y. Jia, *Oxid. Metals* **2020**, 94, 265.
- [18] J. Lu, G. Ren, Y. Chen, H. Zhang, L. Li, A. Huang, X. Liu, H. Cai, X. Shan, L. Luo, *Corros. Sci.* **2022**, 209, 110736.
- [19] W. Kai, W. Jang, R. Huang, C. Lee, H. Hsieh, C. Du, *Oxid. Metals* **2005**, 63, 169.
- [20] P. Y. Hou, Y. Niu, C. Van Lienden, *Oxid. Metals* **2003**, 59, 41.
- [21] R. Christensen, V. Tolpygo, D. Clarke, *Acta Mater.* **1997**, 45, 1761.
- [22] E. Airiskallio, E. Nurmi, M. Heinonen, I. Väyrynen, K. Kokko, M. Ropo, M. Punkkinen, H. Pitkänen, M. Alatalo, J. Kollár, *Corros. Sci.* **2010**, 52, 3394.
- [23] B. A. Pint, J. R. Distefano, I. G. Wright, *Mater. Sci. Eng.: A* **2006**, 415, 255.
- [24] R. P. Oleksak, M. Kapoor, D. E. Perea, G. R. Holcomb, Ö.N. Doğan, *NPJ Mater. Degrad.* **2018**, 2, 25.
- [25] Z. Shen, E. Roberts, N. Saravanan, P. Karamched, T. Terachi, T. Yamada, S. Wu, E. Tarleton, D. E. Armstrong, P. J. Withers, *Acta Mater.* **2022**, 222, 117453.
- [26] D. C. Beaudry, M. J. Waters, G. M. Valentino, D. L. Foley, E. Anber, Y. Rakita, C. J. Brandenburg, J.-P. Couzinié, L. Perrière, T. Aoki, *Sci. Adv.* **2024**, 10, 9697.
- [27] A. Shaik, R. Roy, M. Topping, H. Nordin, S. Y. Persaud, M. R. Daymond, *Corros. Sci.* **2024**, 240, 112420.
- [28] D. Yavas, T. Phan, L. Xiong, K. R. Hebert, A. F. Bastawros, *Acta Mater.* **2020**, 200, 471.
- [29] W. R. Wang, W. L. Wang, S. C. Wang, Y. C. Tsai, C. H. Lai, J. W. Yeh, *Intermetallics* **2012**, 26, 44.
- [30] N. Birks, G. Meier, F. Pettit, *Introduction to the High-Temperature Oxidation of Metals*, Cambridge University Press, Cambridge, UK **2006**.
- [31] D. B. Miracle, J. D. Miller, O. N. Senkov, C. Woodward, M. D. Uchic, J. Tiley, *Entropy* **2014**, 16, 494.
- [32] T. Yang, S. Xia, S. Liu, C. Wang, S. Liu, Y. Zhang, J. Xue, S. Yan, Y. Wang, *Mater. Sci. Eng.: A* **2015**, 648, 15.
- [33] J.-Y. Kim, J. R. Greer, *Acta Mater.* **2009**, 57, 5245.
- [34] A. M. Z. Tan, Z. Li, H. Gao, *Phys. Rev. Mater.* **2023**, 7, 053601.
- [35] Q. Zhang, R. Huang, J. Jiang, T. Cao, Y. Zeng, J. Li, Y. Xue, X. Li, *J. Mech. Phys. Solids* **2022**, 162, 104853.
- [36] H. Ren, R. Chen, T. Liu, X. Gao, G. Qin, S. Wu, J. Guo, *Appl. Surf. Sci.* **2024**, 652, 159316.
- [37] J. Lu, Y. Chen, H. Zhang, L. Li, L. Fu, X. Zhao, F. Guo, P. Xiao, *Corros. Sci.* **2020**, 170, 108691.
- [38] J. Nychka, D. Clarke, *Oxid. Metals* **2005**, 63, 325.
- [39] B. Pint, *Oxid. Metals* **1996**, 45, 39.
- [40] E. Vivas, D. Peña Lara, G. M. Alvaro, *Ionics* **2021**, 27, 781.
- [41] G. Gibbs, R. Hales, *Corros. Sci.* **1977**, 17, 487.

- [42] M. Brumm, H. J. Grabke, *Corros. Sci.* **1993**, *34*, 547.
- [43] C. Desgranges, F. Lequien, E. Aublant, M. Nastar, D. Monceau, *Oxid. Metals* **2013**, *79*, 93.
- [44] E. O. Kirkendall, *Trans. Aime* **1942**, *147*, 104.
- [45] S. Qiu, X.-C. Zhang, J. Zhou, S. Cao, H. Yu, Q.-M. Hu, Z. Sun, *J. Alloys Compd.* **2020**, *846*, 156321.
- [46] S. Perusin, B. Viguier, D. Monceau, L. Ressier, E. Andrieu, *Acta Mater.* **2004**, *52*, 5375.
- [47] S. Plimpton, *J. Comput. Phys.* **1995**, *117*, 19.
- [48] S. Alexander, *Modell. Simul. Mater. Sci. Eng.* **2010**, *18*, 015012.
- [49] Y. Wu, Z. Bai, G. Yan, W. Yu, S. Shen, *Int. J. Refract. Metals Hard Mater.* **2024**, *125*, 106885.